A reciprocal 360-degree 3D light-field image acquisition and display system

ALİ ÖZGÜR YÖNTEM[1], KUN LI[1], AND DAPING CHU[1,*]

[1] Centre for Photonic Devices and Sensors Group, University of Cambridge, 9 JJ Thomson Avenue, Cambridge CB3 0FA, United Kingdom
[*] Corresponding author: dpc31@cam.ac.uk

Compiled December 24, 2018

A reciprocal 360-degree three-dimensional light-field image acquisition and display system was designed using a common catadioptric optical configuration and a lens array. Proof-of-concept experimental setups were constructed with a full capturing part and a truncated display section to demonstrate that the proposed design works without loss of generality. Unlike conventional setups, which record and display rectangular volumes, the proposed configuration records 3D images from its surrounding spherical volume in the capture mode and project 3D images to the same spherical volume in the display mode. This is particularly advantageous in comparison to other 360-degree multi-camera and multiple projector display systems which require extensive image and physical calibration. We analysed the system and showed the quality measures such as angular resolution and space bandwidth product based on design parameters. The issue due to the pixel size difference between the available imaging sensor and the display was also addressed. A diffractive microlens array matching the sensor size is used in the acquisition part whereas a vacuum cast lens array matching the display size is used in the display part with scaled optics. The experimental results demonstrate the proposed system design works well and in good agreement with the simulation results.

http://dx.doi.org/10.1364/ao.XX.XXXXXX

1. INTRODUCTION

Holography is a very well-known technique for true 3D image acquisition and display [1]. However, it has fundamental drawbacks preventing it being widely available for out of the lab applications [2]. Integral imaging is an auto-stereoscopic and multi-view method used for 3D imaging and display under incoherent light illumination [3]. It can overcome conventional stereoscopic and auto-stereoscopic display limitations and many advances in this technology have been demonstrated [4]. Moreover, it has been shown that this method is indeed related to holography [5]. Light-field imaging [6–8] is rapidly developing as an alternative to conventional methods [9]. A light-field is mathematically defined as a 4D function, which gives the positional and directional intensity distribution [10]. A 3D light-field system can potentially record and display high-resolution 3D images compared to integral imaging. It has also been shown that light-field is equivalent to integral imaging when certain restrictions are imposed on the light-field data [11]. In this paper, we will base our design on the assumption that these two methods are similar. One important similarity between the integral imaging and light-field imaging is the capturing and displaying methods used in these systems. Figure 1 shows a generic approach for recording and displaying rays using a microlens array. The directions of the arrows are shown for both capture and display parts. The plane of microlens array (u,v) and the plane of recording (s,t) are assumed to be equivalent to the planes describing a 3D light-field. However, when a microlens (or alternatively a pinhole) array is used, only those rays passing through the centre of each lens array are recorded. Therefore, we have a subset of the whole light-field data.

It is possible to capture the light-field data using multi-camera array systems or single sensor camera with micro-lens arrays, depending on the application needs [9]. A plenoptic camera can be used to image the 3D light-field data. A focused plenoptic camera has a main lens, which images the scene/object onto an intermediate imaging volume. This focused image is then imaged a second time by the microlens array onto the camera sensor [12]. Acquisition part is relatively straightforward compared to display part. The captured data can be used for numerical reconstructions and computational refocusing, [13, 14].

Unlike generic integral imaging displays, the 3D light-field displays are demonstrated using a directional diffuser screen [17] or complex parallax barrier methods [18]. In these approaches, the common goal is to recreate the directional light rays. Scanning type displays can demonstrate 3D images in a cylindrical 360-degree volume, whereas integral type displays would generate 3D images in a limited angular section [17]. The

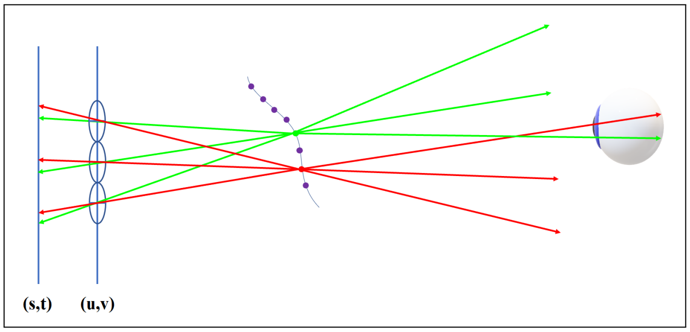

Fig. 1. A generic light-field data recording and display method using microlens arrays. Arrows towards (s,t) plane represents recording, and away from (s,t) plane represents display parts.

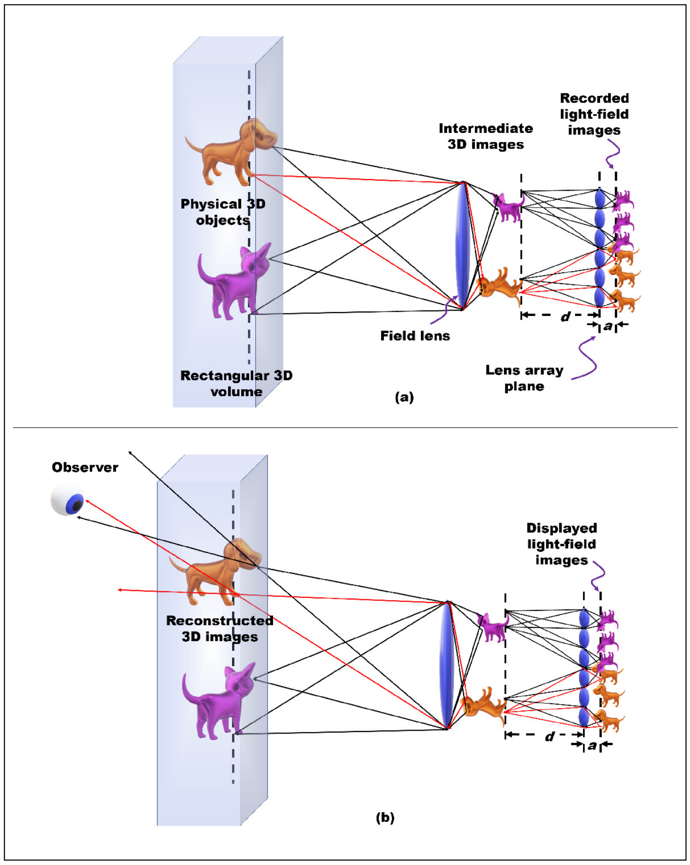

Fig. 2. A generic light-field system for 3D image (a) acquisition and (b) display based on focused plenoptic camera configuration.

scanning type light-field displays are fundamentally limited as they require mechanical movement. Integral type displays require multiple projectors to display in a rectangular volume. Although they can be configured to display 3D images in a full 360-degree or truncated cylindrical volume as in scanning type, they are quite bulky.

Generic 3D light-field acquisition, based on focused plenoptic camera [19], and reciprocal display systems are planar configurations which generate 3D images in a rectangular volume as depicted in Fig. 2 (a) and (b). The reciprocity in integral imaging based capture and display systems were studied earlier [20–22] in different context. The common aim was to record and display a live stream of 3D data. However, these 3D display systems provide only a limited field of view within a limited viewing angle.

It is desirable to be able to record and display 3D images in a 360-degree volume. There is a trending demand and work on 360-degree camera systems [23] which offer a new way of image acquisition especially for virtual reality content creation. However, most of these designs require bulky and expensive multi-camera rigs with sophisticated calibration procedures. In addition, they require extensive image and physical calibration with planar approximation of hypothetical spherical sensors [24]. In addition, several recent optical designs with 360-degree displays have been demonstrated. Nonetheless, one the design requires multiple imaging sources configured around a small 3D volume [25], while the other does display in the free space at all [26].

We have recently reported a novel design for a 360-degree 3D light-field system with a single plenoptic camera and a display [27] which uses a common optics to record and display 3D images. Here in this paper, we expand te design with a more detailed optical analysis, simulations, physical experiments, and the discussion of challenges arose during system demonstration. Our initial design aimed to have a reciprocal optical acquisition and display structure as shown in Fig. 3. A catadioptric optical relay system, i.e. a parabolic mirror and a field lens combination, will first image a surrounding 3D volume to an intermediate imaging volume. Then, a beam-splitter would allow a sensor to capture the 3D information present as depicted in Fig. 3 (a). Our design assumes exact matching of physical sensor and display parameters. Hence, the captured information would be processed, and then displayed through the same beam-splitter. Therefore, 3D images could be relayed back to the exact same locations as their 3D object counterparts. Due to the practical limitations, such as the difference between the pixel size and count between the camera sensor and the display, we separated sub-systems and demonstrated the results independently. The "360-degree" property of our design is in the sense that the system captures from and displays to the same surrounding volume. This is different from other systems, such as the one demonstrated in [28] which captures the 360-degree information around the 3D object with a light-field camera and two planar mirrors and reconstructs the 3D information using a holographic display. The use of the curved mirror is also studied in different cases such as the one in [29]. A hyperbolic mirror was placed in front of a conventional camera to capture 360-degree circumference in a single shot, and a numerical 3D reconstruction of a recorded scene was demonstrated using light-field calculation techniques. In our case, our system captures the light-field data intrinsically using the lens array. Another work, [30], is published just after our reported study, where a parabolic mirror is used to create a 360-degree image by making use of holographic reconstruction. Although this work has a similar aim to our method, it does not include the capturing stage which would be extremely difficult if holographic methods would be used for recording.

We structured the paper as follows. In Sec. 2, we demonstrate design principles and constructed optical setups. In Sec. 3, we model and simulate the design with certain parameters. In Sec. 4, experimental results are presented based on these physical parameters. Finally, we discuss the limitations and potential improvements of the system and draw our conclusions.

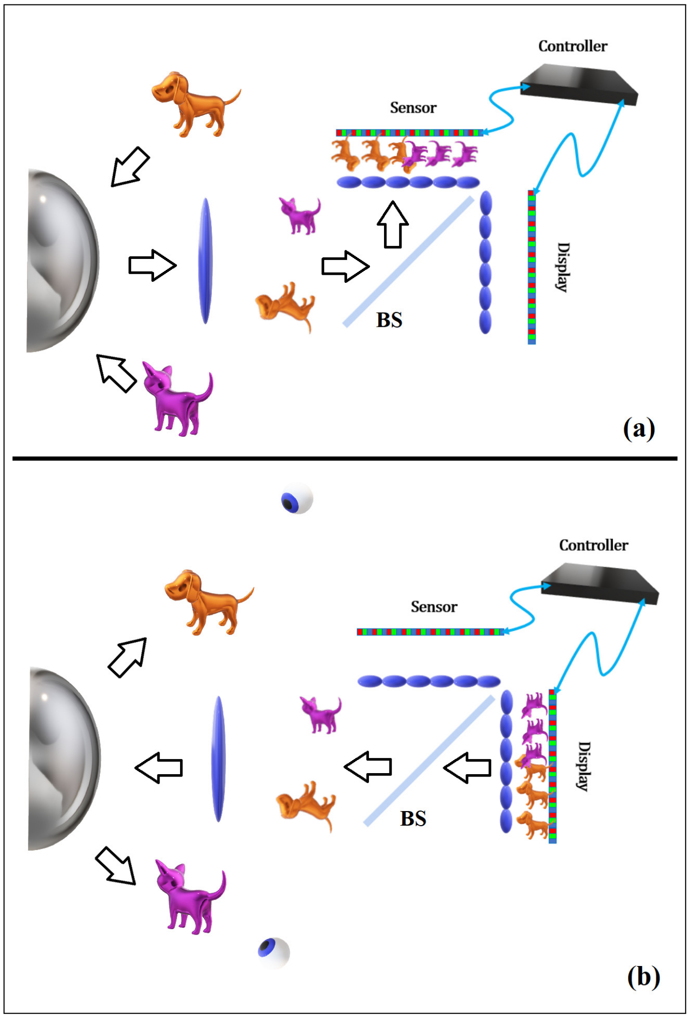

Fig. 3. A reciprocal 3D light-field acquisition and display system design with common optics. (a) Capturing. (b) Displaying. Arrows indicate the direction where the light rays travel. Left side of each sub-figure is assumed to have the catadioptric optics.

2. 3D LIGHT-FIELD ACQUISITION AND DISPLAY SYSTEM DESIGN

Our proposed system can record a spherical volume around itself and display the true 3D images of the objects in their respective physical places as shown in the conceptual sketch in Fig. 4 (a). Acquisition and display parts of the proposed system are shown in Fig. 4 (b) and (c), respectively. In both setups, a single conventional 3D light-field acquisition/display device is used to record/display all 360-degree information. The display can project multiple 3D images to multiple observers. Alternatively, a single 3D image can also be displayed, and an observer can view different parts of the same 3D image. Our system design exploits catadioptric optical systems [31] together with a diffractive optical element (DOE). An array of DOE microlenses, which have smaller diameter and shorter focal length compared to conventional ones, offers a compact low-cost solution for capturing high resolution light-field images even under incoherent light illumination. The common reciprocal optical configuration allows to record from its surrounding volume in the capture mode and project 3D images to the same volume in the display mode when the sensor at the imaging plane is replaced by a display.

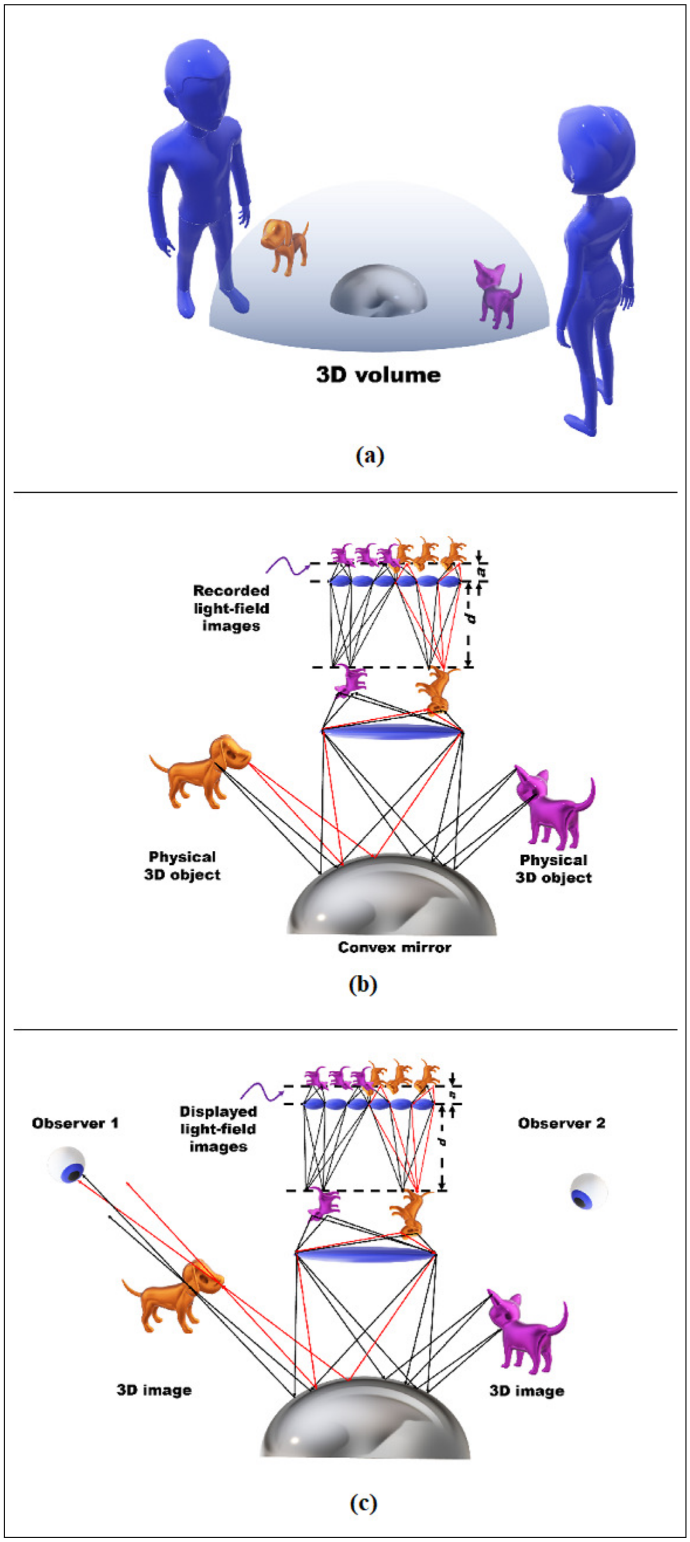

Fig. 4. Proposed design for a (a) 360-degree 3D light-field system in display mode. The 3D images are being displayed in a spherical volume rather than a rectangular volume. (b) The light-field camera and (c) display of the proposed design.

A. 360-degree 3D light-field camera design

The microlens array of the capturing part is the crucial optical component which is normally manufactured by conventional methods. However, the design and manufacturing of these components are significantly costly. Using off-the-shelf microlens arrays is an option although it is not cost effective and more importantly, with their fixed physical catalogue parameters, it will be a limiting factor in the overall system design. Therefore, alternative approaches, such as diffractive optical components, would better fit in the proposed design case. It has been shown that diffractive lenses, realised as binary masks or by reconfigurable spatial light modulators, can be used to replace conventional microlens arrays [32, 33]. Although binary masks might give low diffraction efficiency, phase-only liquid crystal on silicon devices will give significantly better-quality results [5].

In [14], a focused plenoptic camera design to record high quality light-field images is demonstrated. An off-the-shelf high-resolution camera and a manual lens pair is converted to a plenoptic camera by inserting a micro photon sieve array (mPSA) between the lens and the camera sensor. Based on this camera design, our proposed 360-degree light-field camera design comprises this focused plenoptic camera and a parabolic mirror with a geometry which can collect the light from the volume surrounding it. The field lens and mirror combination can also be regarded as a catadioptric imaging system which images a large surrounding 3D volume in front of a microlens array, which captures sub-images of the scene/objects in the imaged 3D volume, as in a conventional integral imaging setup [3].

B. 360-degree 3D light-field display design

In principal, the display part traces all the rays in the reverse optical path of the acquisition part because of the common optical configuration. Therefore, the light rays would be as if they are coming from the original object. The proposed system is similar to an integral imaging display. However, the additional mirror helps to cover the surrounding volume. The rays from different objects are recorded from different angles. The replayed rays will reconstruct the objects in their original physical locations as real images. Hence, the observers will be able to visualise the objects from their respective positions as in Fig. 4 (c). One example geometry for the mirror can be a convex shape as shown in Fig. 4, although it may not be the optimal geometry.

The reader should note that the optimization of the mirror geometry and the optical setup is out of scope of this paper and left as a future study. The mirror may introduce certain distortions to the relayed images from the intermediate imaging volume. It should be noted that the distortions incurred on the images this way, can be corrected using additional optics or by image processing. A simple convex mirror will create divergent rays. However, with additional optics it is possible to control the rays to converge. In the display part, all the rays assumed to travel back the same optical path although we do not have all the rays recorded with their exact directional information. The conventional 2D displays scatter the light with a certain angle. We assume that at least two rays from the source will trace back to the desired direction as convergent rays to create a point, while others can be considered as a background noise on the reconstructed image.

It is also possible to computationally generate the light-field images and use the display part only. Ideally, apriori information on the optical distortion of the system needs to be known such that a pre-distortion can be applied on the generated light-field data. If this pre-distortion is not applied, an image reconstruction will still be possible with some distortion.

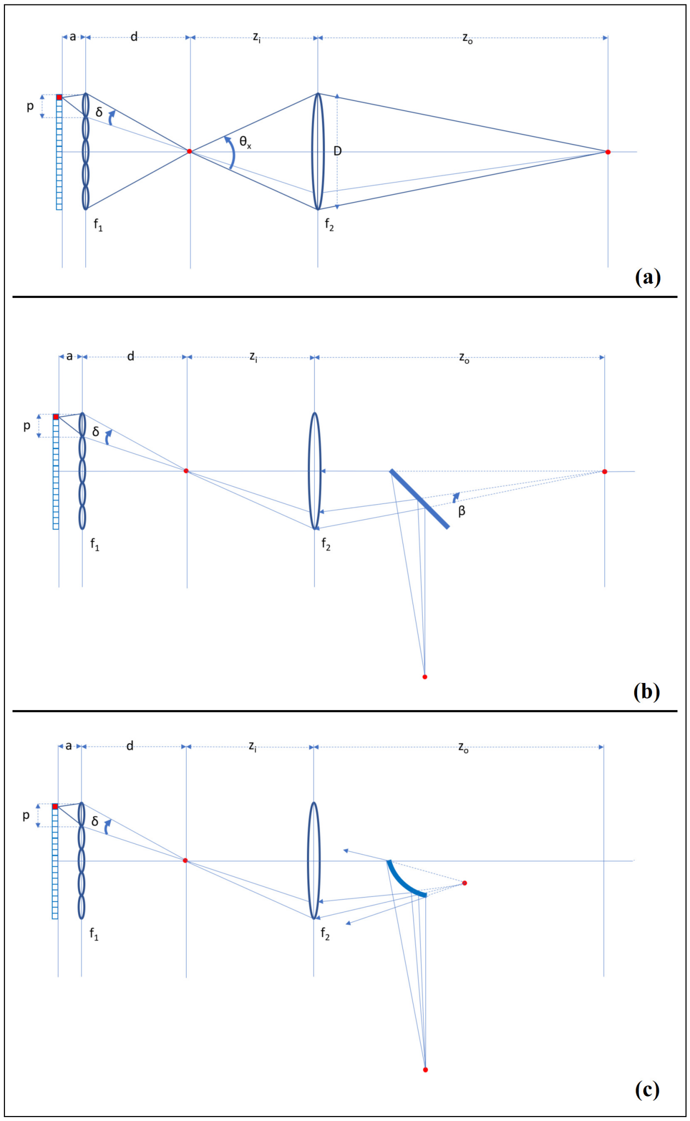

Fig. 5. Schematics of a light-field capture system are shown (a) without a mirror, (b) with a (half) conical mirror, and (c) with a (half) parabolic mirror.

One major practical issue we had in the display part is the pixel size mismatch between the camera sensor and the display. Due to this difference, we had to construct a scaled setup for the display part. A 4K mobile phone (Sony Xperia XZ Premium) screen used to display approximately a quarter of the entire image captured by the 8K×5K full frame camera sensor. A matching lens array is designed in house based on the design rules given by [16] and manufactured by Materialise UK Ltd, using vacuum casting method. Each element in the array has a 7mm×7mm size with a focal length of approximately 32mm. The manual camera lens is replaced by a stack of Fresnel lenses. A single Fresnel lens, with a 300mm focal length and 300mm diameter, did not give f-number required to bend the rays towards the edges of the parabolic mirror. Therefore, with a stack of three Fresnel lenses we achieved one third of the focal length of a single lens while maintaining the same aperture size. With the large lenslet size and long focal length, the reconstructed images create a coarse 3D reconstruction when it passed through the Fresnel lens stack.

C. Analysis of the designs

In this sub-section, we give a basic analysis of this complex system. A detailed analysis can further be carried out together with the optimization of the system.

In Fig. 5 (a), we start with a conventional light-field capturing setup. At this stage, we assume circular symmetry around the optical axis. A point source at the object reference plane will be imaged by a field lens to the intermediate imaging plane. Then, the image at the intermediate imaging plane will be captured by individual microlenses and mapped to the pixels of the sensor. Assuming that the point source at the object reference plane has Lambertian scattering, the field lens will be able to collect only a portion of the uniformly distributed light rays it receives. The total angle, θ_x, will be determined roughly by the numerical aperture, f_2/D, of the lens. However, we will use the imaging distance parameter, z_i, instead. The rays will then travel with this limited angle and reach to the microlens array, where the rays will further be limited, δ, and then be imaged on the sensor. If the number of the microlenses receiving the rays from the field lens in the array are M_x, then;

$$\theta_x = 2 \times atan(D/2z_i) \ and \ \delta = \theta_x / M_x. \tag{1}$$

δ gives the angular resolution of the capturing system. To find the spatial resolution, we need to determine the point spread function of the microlenses, which will be given by $1.22 f_1 \frac{\lambda}{p}$ for a diffraction limited lens, where f_1 is the focal length, λ is the wavelength and p is the diameter. If the pixel size of the sensor is smaller than this value, there will be no one-to-one mapping of the points which reduces the captured image resolution and it is the case for these systems. However, for mathematical point of view we will assume we can record the rays individually by a single pixel.

In the display stage, we replace the sensor with the display and we trace the rays back to the object plane from the display pixels. The pixel period of the display normally determines the spatial bandwidth, and the number of pixels determine the spatial extend. These two parameters will give the space-bandwidth product (SBP) of the display system, which is a measure used to quantify the performance of the holographic displays [34–36]. This can be extended in our case. However, we cannot apply the same definition on the display as the holographic displays because the pixels on the display will be imaged through the microlens array which decreases the spatial extend and limits the spatial bandwidth. In this case, we can define the SBP on the intermediate imaging plane. The angular resolution δ will give the spatial bandwidth and the number of points imaged by a single lens will give the spatial extend, $N_x \times 1.22 f_1 \frac{\lambda}{p}$, where N_x is the number of pixels that a single lens images. Therefore, we can approximate

$$SBP = \frac{2 \times atan(D/2z_i)}{M_x} \times 1.22 \times \frac{f_1 \lambda}{d} \times N_x. \tag{2}$$

If we place a conical mirror between the field lens and the object reference plane, it will change the direction of the imaging as shown in Fig. 5 (b). The rays from a point source on the object reference plane will expand in a conical volume and will be reflected from the mirror surface. However, we will still have a similar imaging performance if we assume that the solid angle of the conical volume is small enough to be regarded as a ray. (On a certain plane cut, the angle would be β.) Moreover, we will be able to capture the 360-degree periphery of the surrounding volume. The rectangular field of view of the system will be translated to a spherical one. However, this will not increase the SBP of the display system simply because the parameters of the system did not change.

The more complicated situation is when we place a parabolic mirror as depicted in Fig. 5 (c). In this case, the ray bundle coming from the object point will assume a more divergent path. The convex mirror will create a virtual point at a closer distance than the origin of the point. Moreover, this will create a distortion on the virtual image. In this case, a narrower ray bundle will be reaching to the field lens. Therefore, the information density from the object point will be decreased.

Although in the display stage it is possible to reconstruct the 3D image by reversing the ray paths, the quality of the image will be decreased in the case where a mirror is used.

3. DESIGN VERIFICATION AND SIMULATION RESULTS

Optical simulations are carried out using ZEMAX to explore and verify the optical design. The light source used in the simulations is a 2D rectangular LED, in which the emitting angle and light distribution can be controlled by varying the model parameters. Light is uniformly emitted from the source surface at the designed angle and intensity distribution. The optical components are simulated with paraxial lenses, so the wavelength of light rays within the visible range does not have an effect on the ray tracing results. The default design wavelength of 550nm used for all ray tracing simulations.

A. Simulation of the acquisition part

The schematics of acquisition setup is illustrated in Fig 6 (a). The LED light source with a dimension of 101mm× 101mm and a diverging angle of 30° (FWHM) is used as the object. Three black stripes, each of 20mm× 100mm, are placed right in front of the LED source and they block light rays from the covered sections. A ZEMAX 'standard surface' is used as the parabolic mirror. The radius of curvature is set to 338.4mm and the conic constant set to (-1), these values match the physical dimensions of the real component. The camera/field lens has a maximum effective aperture of 11.1mm in diameter and it is simulated as a paraxial lens. A paraxial lens array is used to simulate the mPSA. The camera sensor (Sony A7R II, 42 MPx) has a dimension of 24mm×36mm and resolution of 7952×5304 with a pixel size of 4.52μm. In ZEMAX, it is simulated as a 'detector' and the smallest pixel size with the given dimension is 6μm.

The distance between the lens array and the camera sensor is fixed to the imaging distance of 12.5mm. The LED light source (object) is about 270mm away from the parabolic mirror surface, which is 150mm away from the field lens. The camera lens aperture is set to f/1.8 to allow more light rays collected by the sensor. The simulated image on the detector is shown in Fig. 6 (b) with an inset showing a single enlarged sub-image, all sub-images are clearly seen. Because the object is only at one side of the parabolic mirror, the corresponding sub-images are congregated towards one side of the sensor. The object that is imaged can be as close as 40mm away from the field lens, with its image distance 40mm from the field lens. However, it is observed that an object distance of greater than 100mm gives sharper images on the sensor. An object at infinity would be

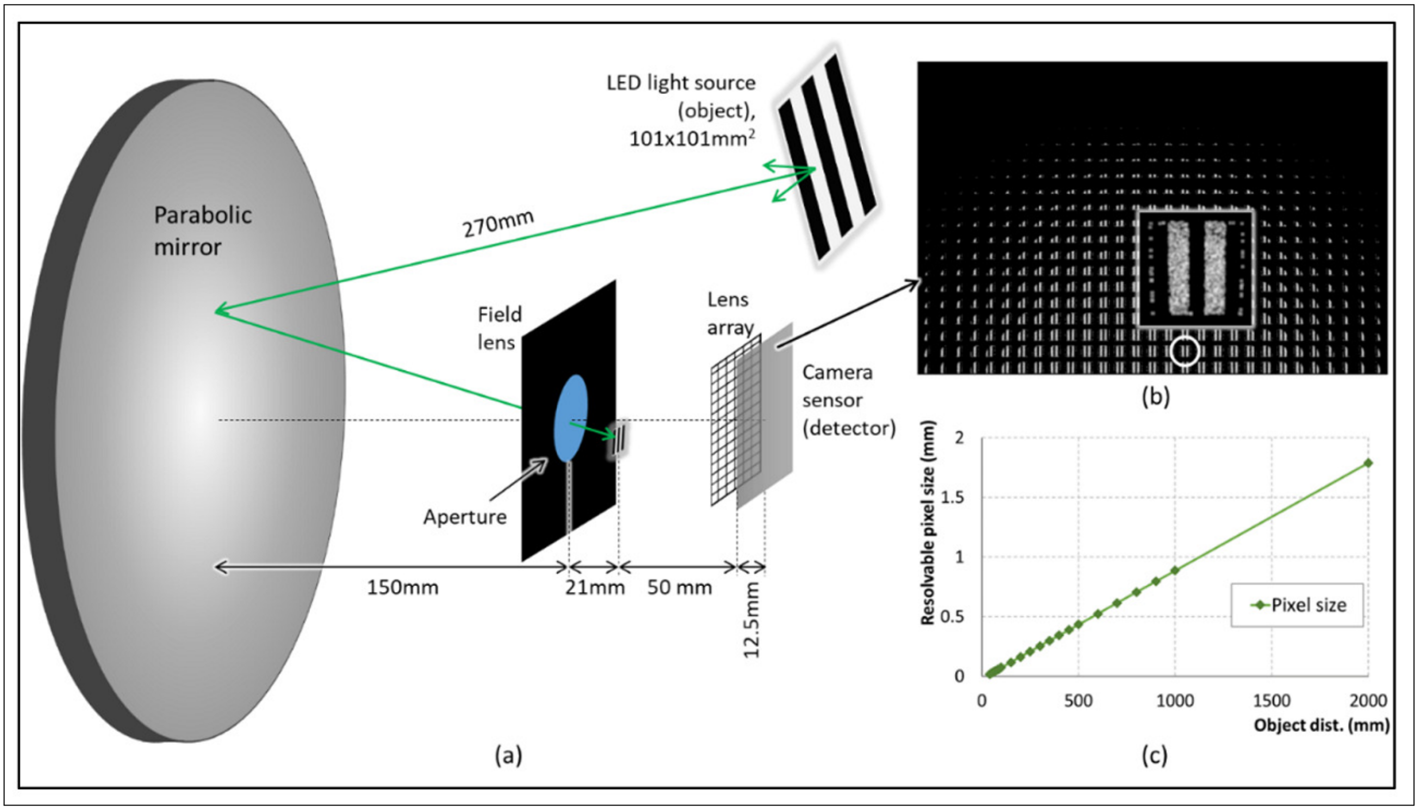

Fig. 6. (a) Schematics of the capture system with a parabolic mirror and a 10mm EFL lens array. (b) Simulated ray-tracing results on the detector. (c) Chart with the minimum resolvable pixel size against the object distance.

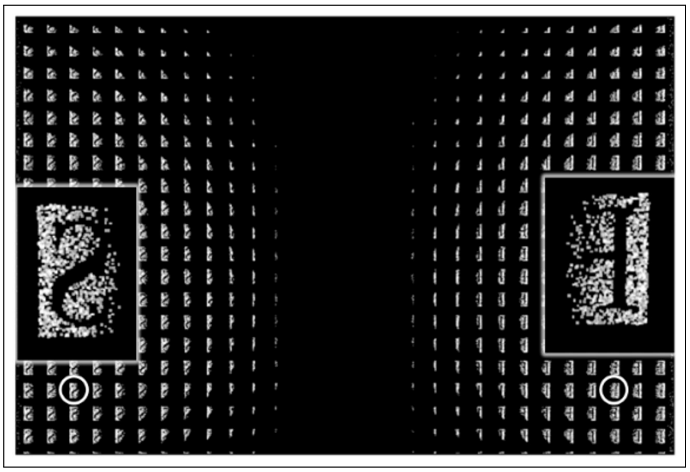

Fig. 7. Simulated image on the detector for the optical setup shown in Fig. 9 (b).

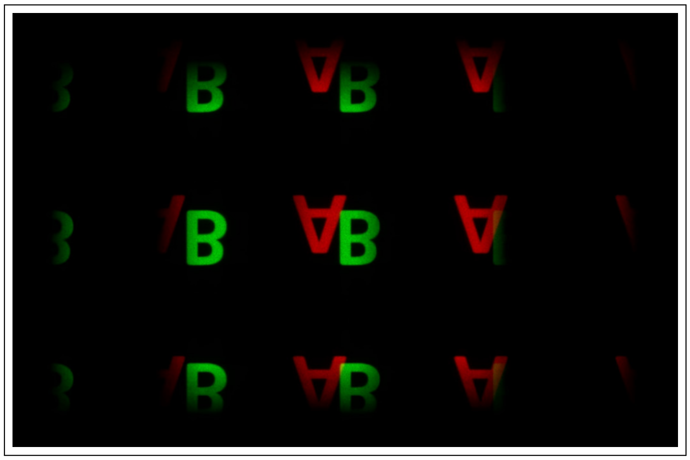

Fig. 8. A set of sub-images with different colours and distances are generated using wave propagation.

imaged as a point on the sensor and it will not be possible to resolve its details. With the field lens and lens array in use, the smallest pixel size at the intermediate plane is calculated 18.08μm. An object at 2 metres away would have a resolvable pixel size of 1.8mm, as shown in Fig. 6 (c), the resolvable pixel size increases linearly with the object distance.

Two different letter shaped light sources ('F' and 'S') are used as objects in ZEMAX, as shown in Fig. 9 (a). In simulations, the detector, lens array, camera/field lens, and parabolic mirror are placed at the locations shown as in Fig. 6 (a). A lens entrance aperture with a diameter of 70mm is inserted to mimic the real camera lens, and the two objects are symmetrically placed on either side of it with a distance of 70mm from the parabolic mirror. The simulated (captured) sub-images of two letters are clearly seen in Fig. 7. Since both letters are symmetrically placed around the camera lens optical axis, their sub-images are imaged symmetrically on the camera sensor.

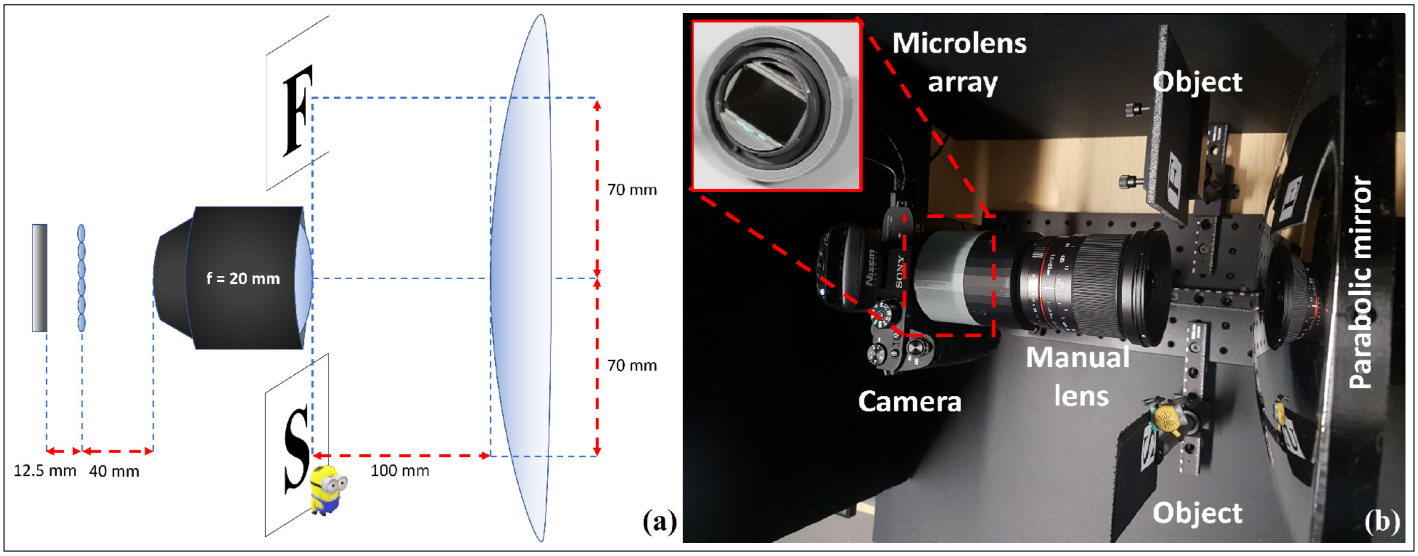

Fig. 9. (a) The Schematic of the capturing setup. (b) The physical capturing setup.

B. Simulation of the display part

The schematics of display setup is illustrated in Fig. 10 (a). The same rectangular LED source, that is used in imaging simulation, is used here to simulate a 4K mobile display (Sony Xperia XZ Premium, ≈ 807 ppi density). The LED source has a 5° full-width half-maximum diverging angle so that most of light rays go through the corresponding lens, although in practice the mobile display has a much larger scattering value.

As the test image, the sub-image set shown in Fig. 8 is generated. Two different colour letters, ’A’ and ’B’, at two different depths are generated using wave propagation. In [15], a method to convert pseudoscopic images to orthoscopic images was given. A 3D data set was input to a two-step wave propagation algorithm. In that, it is shown that the points on the reference plane should be imaged closer to each other compared to the points at the far away plane. For example, a 2D letter on the closer plane should be imaged as smaller sub-images whereas a 2D letter at the far away plane should have larger images. Therefore, when the 3D reconstruction is done, the corresponding images appear in the right order. In this paper, in the generation of the sub-images, we obtained the images at the same distance both for ’A’ and ’B’ in order to generate an all in-focus image set. Obviously, the physical reconstructions of the objects would be at the same distance if we used this sub-image set directly. Therefore, the sub-images of the letter ’A’ slightly (less than 10%) enlarged in size. This brought the physical reconstruction distance closer to the lens array while keeping the resolution of the images high. Therefore, we obtained orthoscopic reconstruction of the sub-image set. For the ZEMAX simulations, the sub-image set for each letter was separated from the combined images. Each sub-image set for each letter was input to the simulations separately.

An effective section (9×9 elements) of the larger lens array (10×18 elements) is simulated as an array of paraxial lenses, each with a square period of 7mm×7mm and the EFL of 29.7mm. The EFL is different from the designed value of 32mm, which the physical lens array was fabricated by vacuum casting and has a thickness of 5.5mm. The simulated paraxial lens on the other hand does not have a thickness, in order to address this difference, a different EFL value is chosen in the simulation to produce the same imaging distance as the experimentally obtained one. As mentioned in Sec. 2, three identical Fresnel lens are placed close to one another and used as the field lens, with each Fresnel lens having an EFL of 300mm. The resultant EFL is 102.6mm. The field lens is simulated as a paraxial lens. Such an arrangement provides a small f-number of ≈ 0.34 and can reduce the volume of the display system.

The same parabolic mirror from the imaging simulation is used in the display simulation. The distance between each part of the display system is annotated in Fig. 10 (a), and the simulated images are included as insets to the location where detectors are placed.

With the setup of 42mm between the sub-images and lens array, the integrated images of letter ’A’ and ’B’ are formed at 93mm and 108.5mm away from the lens array, respectively. The reconstructed images are then relayed by the field lens and the parabolic mirror to the viewer’s direction. The letter ‘A’ seen from the viewer’s point of view is about 103mm from the intersection of light rays and parabolic mirror, while the letter ’B’ is about 208mm away. The final simulated images are shown as ‘Simulated images’ in Fig. 10 (a), they are about 3.9 times of the displayed sub-images for ’A’ and 7.8 times for ’B’, respectively.

4. EXPERIMENTAL RESULTS

After design verification by simulations, we conducted physical experiments to confirm and qualify the actual setups. Note that in the demonstration of the display part, the setup was limited by the available components at the time of the experiments. It should be obvious to the reader that the display and the lens pair can be rotated around the optical axis to display from other angles to demonstrate another 3D image from a different viewing point since the mirror will be circularly symmetrical around the optical axis. In our case, in order to match the captured image size, we would need at least four 4K mobile screens and matching lens arrays to be able to cover most of the mirror surface from all angles in a 360-degree circumference.

A. Acquisition part experiments

Figure 9 (a) shows the schematic of the 360-degree camera setup and Fig. 9 (b), shows the physical camera setup. Objects are

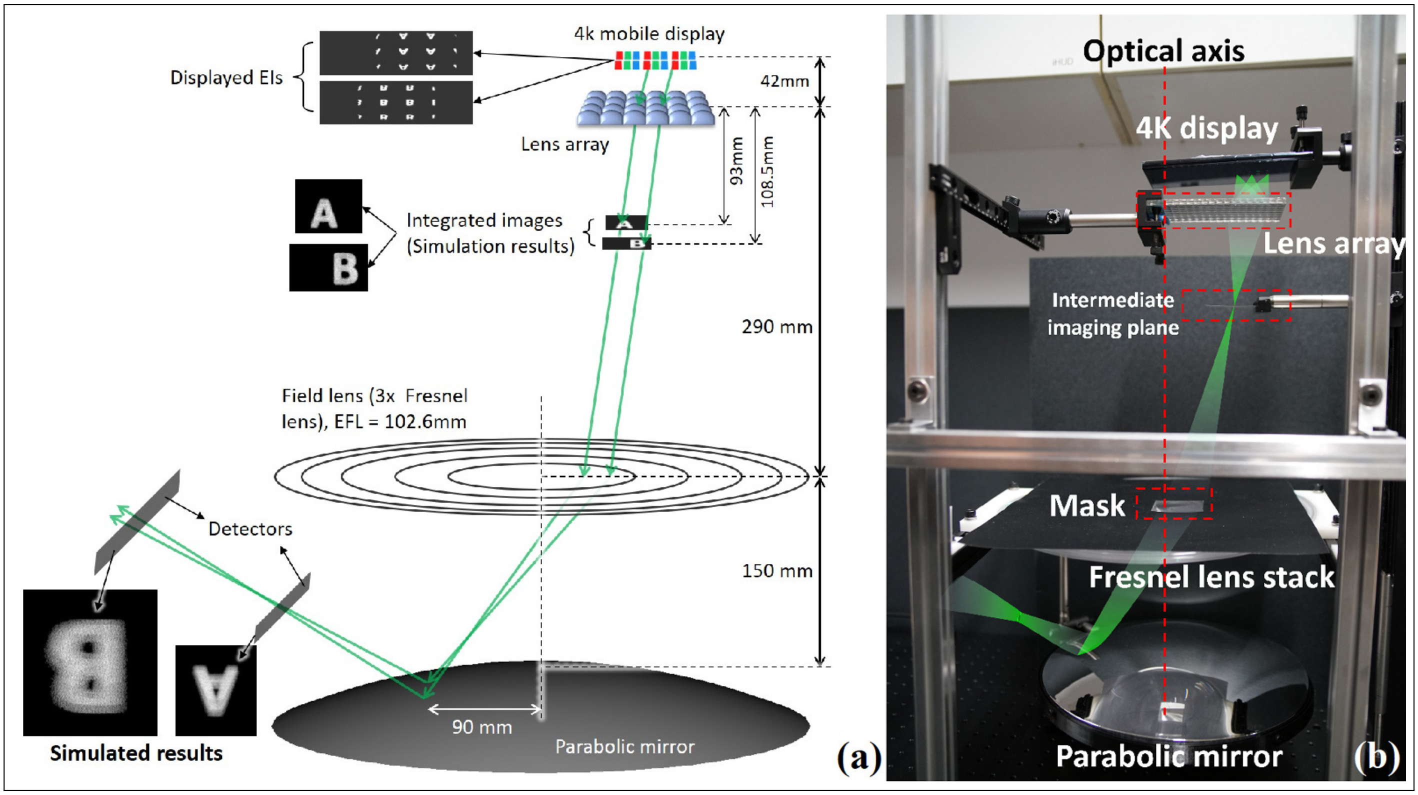

Fig. 10. (a) Schematics of the displaying part with the sub-images and lens array, with simulation results (insets) of the integrated image at the intermediate plane and the viewer's plane. (b) The Display setup. A 4K mobile phone display (Sony Experia XZ) is used to display 2D sub-images. A lens array, fabricated by vacuum casting with 10×18 elements and 32 mm focal length each, matching the displayed sub-images is used to reconstruct the 3D images. A stack of Fresnel lenses with a focal length and diameter of 300mm is used to obtain a low f-number equivalent lens. A parabolic mirror, used to mitigate the blind spots in traffic, with 300mm diameter is placed after the Fresnel lens stack.

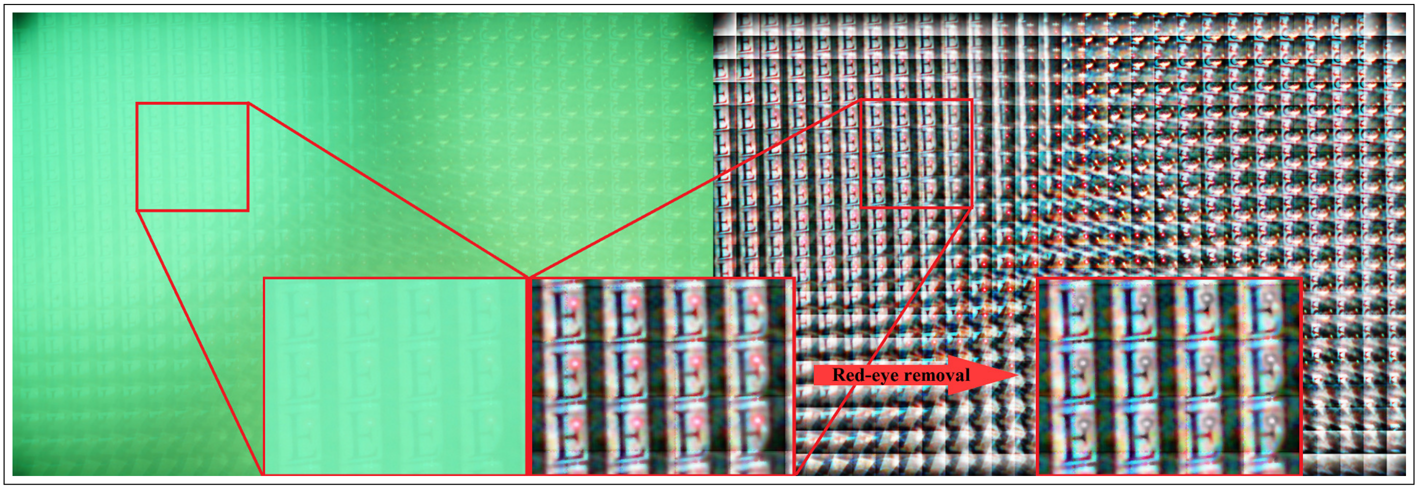

Fig. 11. The captured (left) and processed (right) sub-image sets. Insets on the left and in the middle show the portions from corresponding images. The one on the right shows after red-eye removal applied. Although we have recorded the images using green colour filter, we obtained full colour images after the processing steps. This is due to the poor spatial filtering of the filter used over the flash light source.

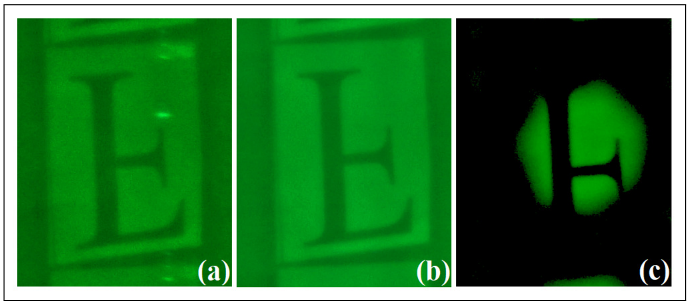

Fig. 12. Single sub-images cropped from the same location of the recorded images with lens aperture size of (a) f/1.8, (b) f/4 and (c) f/11.

placed on either side of the parabolic mirror. The reflected images are imaged using the manual lens (Samyang 20mm F1.8 ED AS UMC) to an intermediate imaging volume. This volume is imaged onto the (42Mpx, 8K×5K) camera sensor using the (33×21 element) mPSA with each element having a focal length of 10mm and a diameter of $\approx 1mm$. The mPSA is designed for a single wavelength, λ = 532nm.

Using the setup in Fig. 9 (b), we captured the sub-image set shown in Fig. 11. An external flash light source synchronized with the camera and it is used to illuminate while capturing the images. A green filter is used to partially filter the spatial bandwidth of the light source to bring closer to the mPSA design wavelength. The raw images suffered from some undiffracted light. Due to this, similar image processing steps in [14], are applied on the raw images in order to improve the visibility of the sub-images. We added one extra step to remove the red points appeared due to the flash light reflected from the mirror surface. Since the red dots resemble "red-eye" effect when the subject is a person, we used a manual red-eye removal tool to get rid of this degradation. The processing steps are as follows: 1. Separate each colour channel of the image. 2. Apply a local histogram equalisation over the sub-images. 3. Apply Wiener filtering over the sub-images. 4. Apply red-eye removal at the bright red spots on the image where necessary.

In Sec. 3, all the simulations are done with large camera aperture of f/1.8 in order to have more rays hitting the detector. A wide aperture field lens allows more light to enter to the optical system while forming sharper images in the intermediate imaging volume. However, in the physical experiments, due to the low diffraction efficiency of the mPSA, the captured sub-images will suffer from the background noise because of the high intensity light used for illumination even with low ISO settings. Therefore, the size of the aperture should be chosen such that the undiffracted light is reduced to allow the sub-images to be seen clearly. The effect of the aperture size on the captured images is shown in Fig. 12. With f/4, the letter 'F' has a sharper edge than that of f/1.8, but with f/11, half of the letter is lost due to limited number of light rays entering the camera.

B. Display part experiments

The test image in Fig. 8 is displayed on the mobile phone display. In order to demonstrate the 3D reconstruction with the data, we placed a diffuser at two different imaging distances after the lens array and recorded the reconstructed images shown in Fig. 13 (a) and (b). We later demonstrated the real image reconstruction after the rays are reflected from the parabolic mirror surface. However, we faced one of the limitation of the available optical parts for the demonstration. Figure 13 (c) shows the reflected images from the parabolic mirror surface. The coarse lens array did not provide enough continuous views to reconstruct the entire image and enough rays to make the entire image visible from a single viewing point. Moreover, the parabolic mirror further spread out these limited number of rays which in turn decreased the number of rays entering the camera or eye pupil. Therefore, it required to move the camera or the eye pupil in order to observe the entire reconstructions.

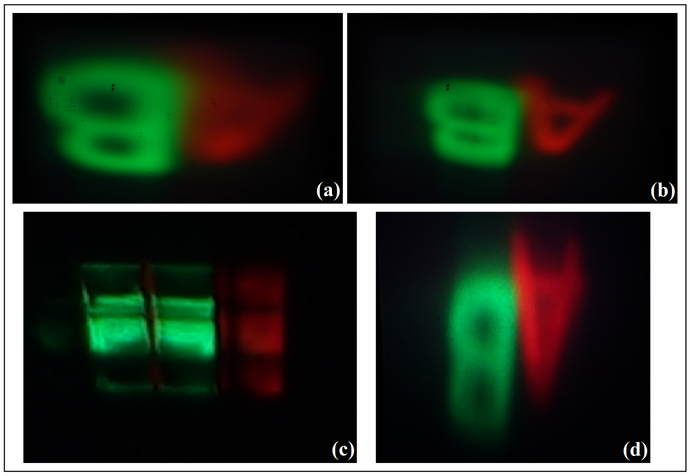

Fig. 13. The reconstructed real images after light rays are reflected from the mirror surface. (a) focus on the letter 'B' and (b) focus on letter 'A' when a narrow angle (15° Luminit) holographic diffuser is placed at the intermediate imaging planes. (c) Observed reconstructed images reflected from the parabolic mirror surface without any diffuser in the intermediate imaging plane. (d) Observed reconstructions realised on the diffuser, which is placed at the reconstruction distance after the rays are reflected from the mirror surface.

C. Displayed image improvement for continuous viewing

Due to the limitations mentioned in the previous sub-section, we placed a simple narrow angle (15°) holographic diffuser at the reconstruction volume after the parabolic mirror to improve the visibility of the reconstructions. This is a similar approach demonstrated in [37]. Each sub-image and the corresponding lens in the array can be regarded as an image projector. The light rays are scattered from the diffuser surface making the reconstructed images visible from wider angles as shown in Fig. 13 (d).

Finally, in order to confirm the reciprocity of the entire system, we used the processed image Fig. 11, captured by the acquisition part given in Fig. 9. We successfully observed a reconstructed real image, Fig. 14, using the display part shown in Fig. 10. We noticed that the use of a largely white background introduces significant colour dispersion which happens as a combined result of the use of a mPSA, poor colour filtering of the display and the parabolic mirror which spreads the rays further. Although, there were many imperfections and difficulty to match the acquisition and display part, we demonstrated that the physical system design works as the numerical verifications. The system can further be improved to mitigate these imperfections with optimized parameters and components.

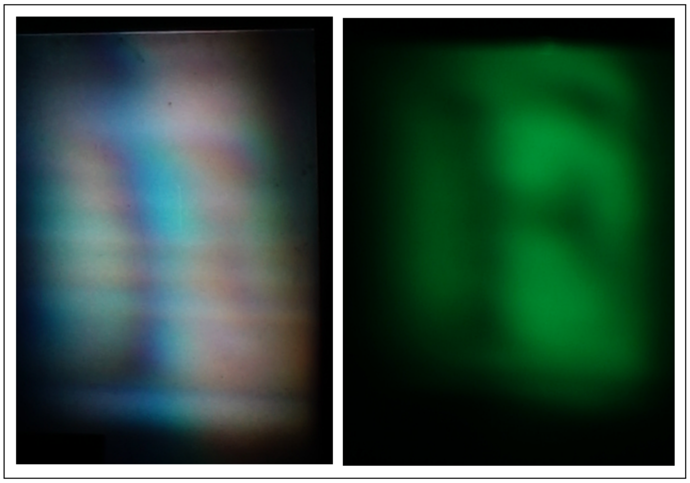

Fig. 14. Reconstruction of the captured image 'F' on realised on a diffuser after it is reflected from the parabolic mirror surface. (left) Full colour. (right) Green colour only.

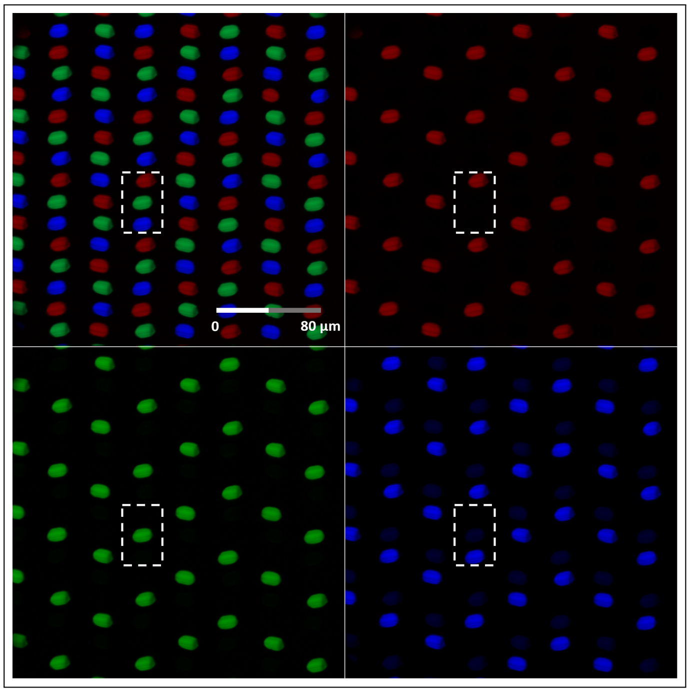

Fig. 15. Display pixel configuration. From left to right, full colour and respective single channel colours isolated from the full colour image are shown. The full colour image is shot under a 60X microscope objective. The dashed boxes represent a single pixel composed of sub-pixels of each individual colour channel. The blue channel leaks through the green pixels. This is visible when the picture is zoomed in.

5. DISCUSSIONS

As demonstrated by the experiments and supporting simulations, the designed system will provide a 360-degree acquisition and display. However, it needs further optimization of the optics and improvement of the image processing steps in order to fully achieve a high-quality 3D image reconstruction. One of the drawbacks is the image sensor and 2D display pixel size mismatch. This is rather a matter of improvements in the available 2D display technologies which is a common problem in any 3D display application regardless of the used approach, i.e. holographic or light-field. The recent developments in the flat panel display technologies, such as LCD and OLED, will enable higher resolution and larger size displays.

Display pixel configuration play an important role for accurate reconstruction of the 3D images. Moreover, the display configuration has to match the capturing sensor pixel configuration. As a common industry standard, a Bayer pattern is used in most of the camera sensors. This is also true for the camera sensor we used according to the basic specification analysis given in [38]. We assume in our work that the stored data is compatible in terms of the image being captured and displayed. However, display part is the physical optical interface effecting the results. Figure 15 shows the display pixel configuration of the display we used in the experiments. There are two important corollaries using this display. Our assumption was that the pixels are arranged in a regular rectangular array. In the actual display, they are arranged in a hexagonal array. Although as a standard display this will reduce artifacts like Moire effects due to small pixel periods and improve the spatial frequency utilisation, we did not take this into account in our optical configuration. The lens array geometry should be configured according to the display pixel configuration for a better pixel-lens utilisation. Secondly, the blue coloured pixels have the worst performance as this colour filter allow partial leakage from the green channel as it can be seen in the right most image of Fig. 15. In fact, there were slight leakage in other channels as well although they were not this severe. This was one of the main problems we had in the reconstruction of the colour images and the main reason in the displayed image quality when Fig. 13 and Fig. 14 are compared. Since we had more image colour control, the reconstructed images of computer generated data resulted in better visibility.

As it is obvious from the above corollaries, the off-the-shelf devices do not provide exactly what is mathematically required although they provide good enough results to prove the concepts. Therefore, these should be considered when optimizing this system. We will also investigate the other possible pixel configurations such as circular ones used in the circular smart watches in our future study.

Another drawback of the current system is two different types of lens arrays used in data capturing and reconstructions. Microlens arrays are crucial components in light-field imaging of the 3D data. Hence, it should be tailored according to the needs of the system. With the new diffractive optical techniques applied to the lens array designs [14], it is possible to achieve better performance in such systems. It will improve the image acquisition and display quality while reducing the size of the systems.

One last drawback in the current system is the parabolic mirror. The main source of the geometric distortions on the images in the system is caused by this component. There are several ways to mitigate the effect of it by optical optimization, digital image processing, or both. The pure optical optimization of the components will be much more complicated in many cases as the system uses unconventional optics. In this case, camera calibration methods in image acquisition and pre-distortion using a known distortion function in image display will be practical.

6. CONCLUSIONS

A 360-degree 3D light-field acquisition and display system was designed and demonstrated using a common optical setup comprising a focused plenoptic configuration and a catadioptric aperture. The use of a paraboloidal mirror is essential for the acquisition and display of a spherical volume surrounding the system. A diffractive optical component, micro photon sieve array, is used as a microlens array in the acquisition part of the proposed design. Due to the difference between the pixel sizes of the acquisition sensor and the display, a scaled version of the acquisition optics is used in the display part. A vacuum cast lens array and a high-resolution mobile phone display are used for reconstructing 3D images. Without loss of generality, a section of the entire image is displayed to demonstrate that the proposed design works. Both the images captured using the proposed design and generated numerically are used in the display setup. The display successfully reconstructed 3D images in their relevant locations as expected. The experimental results were verified by simulations of the system. Such a design is envisaged to be used in video conferencing and immersive gaming.

FUNDING

The research is conducted under the grant "Centre for Advanced Photonics and Electronics - Acorn Blue Sky Research Award 2016".

ACKNOWLEDGMENTS

Portions of this work were presented at the OSA Imaging and Applied Optics Congress in 2018, Design for 360-degree 3D light-field camera and display.

DISCLOSURES

The authors declare that there are no conflicts of interest related to this article.

REFERENCES

1. D. Gabor, "A new microscopic principle," Nature **161**, 777, 1948.
2. P. Benzie, J. Watson, P. Surman, I. Rakkolainen, K. Hopf, H. Urey, V. Sainov, and C. von Kopylow, "A survey of 3DTV displays: techniques and technologies," IEEE T. Circ. and Syst. Vid. **17** (2007).
3. G. Lippmann, "La photographie integrale," C.R.Hebd. Seances Acad. Sci. **146**, pp. 446–451, 1908.
4. X. Xiao, B. Javidi,M.Martinez-Corral, and A. Stern, "Advances in three-dimensional integral imaging: sensing, display, and applications [Invited]," Appl. Opt. 52, Iss. 4, p. 546 (2013).
5. A. O. Yontem and L. Onural, "Integral imaging based 3D display of holographic data," Opt. Express **20**, pp. 24175–24195, 2012.
6. M. Levoy and P. Hanrahan, "Light field rendering," in Proceedings of the 23rd Annual Conference on Computer Graphics and Interactive Techniques, ACM, 1996, pp. 31–42.
7. E. Y. Lam, "Computational photography with plenoptic camera and light field capture: tutorial," J. Opt. Soc. Am. A, vol. **32**, no. 11, pp. 2021–2032, 2015.
8. M. Martínez-Corral and B. Javidi, "Fundamentals of 3D imaging and displays: a tutorial on integral imaging, light-field, and plenoptic systems," Adv. Opt. Photon. **10**, 512-566 (2018).
9. J. Y. Son, H. Lee, B. R. Lee, and K. H. Lee, "Holographic and Light-Field Imaging as Future 3-D Displays," Proc. of IEEE, vol. **105**, no. 5, pp. 789–804, 2017.
10. N. Balram, "Fundamentals of Light Field Imaging and Display Systems," SID, Display Week, (2016).
11. E. Sahin, and L. Onural, "A comparative study of light field representation and integral imaging", Imag. Sci. J., vol. **58**, pp. 28–31, 2010.
12. A. Lumsdaine, and T. Georgiev "The focused plenoptic camera," IEEE ICCP, (2009).
13. J. Tumblin, "Dappled photography: Mask enhanced cameras for heterodyned light fields and coded aperture refocusing," ACM Trans. Graph., vol. **26**, no. 3, 2007.
14. A. O. Yontem, D. Chu, "Design of micro photon sieve arrays for high resolution light-field capture in plenoptic cameras," accepted for publication in Proceedings 3DTV Conference: The True Vision - Capture, Transmission and Display of 3D Video (3DTV-CON), 2018.
15. A. O. Yontem, "Three-dimensional integral imaging based capture and display system using digital programmable Fresnel lenslet arrays," PhD Thesis, Bilkent University, 2012.
16. P. Nussbaum, R. Volkel, H. P. Herzig, M. Eisner and S. Haselbeck, "Design, fabrication and testing of microlens arrays for sensors and microsystems," Pure Appl. Opt. **6**, pp. 617-636, 1997.
17. X. Liu, H. Li,"The progress of light field 3-D displays", Information Display, SID, Display Week, (2014).
18. G. Wetzstein, D. Lanman, M. Hirsch, and R. Raskar, "Tensor displays: compressive light field synthesis using multilayer displays with directional backlighting," ACM Trans. Graph., vol. **31**, no.4, pp. 80:1–80:11, 2012.
19. R. Ng, M. Levoy, M. Br'edif, G. Duval, M. Horowitz, and P. Hanrahan, "Light field photography with a handheld plenoptic camera," Stanford Tech Report (2005).
20. F. Okano, H. Hoshino, J. Arai, and I. Yuyama, "Real-time pickup method for a three-dimensional image based on integral photography," Appl. Opt. **36**, 1598-1603 (1997).
21. Y. Jeong, J. Kim, J. Yeom, C. -K. Lee, and B. Lee, "Real-time depth controllable integral imaging pickup and reconstruction method with a light field camera," Appl. Opt., vol. **54**, no. 35, pp. 10333-10341, 2015.
22. J. Kim, S. Moon, Y. Jeong, C. Jang, Y. Kim and B. Lee, "Dual-dimensional microscopy: real-time in vivo three-dimensional observation method using high-resolution light-field microscopy and light-field display," J. Biomed. Opt., vol. **23**, no. 6, article 066502, 2018.
23. Filmora, "https://filmora.wondershare.com/virtual-reality/top-10-professional-360-degree-cameras.html," (2018).
24. G. Krishnan, S. K. Nayar, "Towards a true spherical camera," Proc. SPIE 7240, Human Vision and Electronic Imaging XIV, 724002, (2009).
25. L. Onural, "Design of a 360-degree holographic 3D video display using commonly available display panels and a paraboloid mirror," Proc. SPIE 10126 pp.10126 – 10126 - 6 (2017).
26. T. Kawakami, M. Date, M. Sasai, and H. Takada, "360-degree screen-free floating 3D image in a crystal ball using a spatially imaged iris and rotational multiview DFD technologies," Appl. Opt. **56**, pp. 6156–6167 (2017).
27. A. O. Yontem and D. Chu, "Design for 360-degree 3D Light-field Camera and Display," in Imaging and Applied Optics 2018 (3D, AO, AIO, COSI, DH, IS, LACSEA, LS&C, MATH, pcAOP), OSA Technical Digest (Optical Society of America, 2018), paper 3Tu5G.6.
28. Y. Jeong, S. Moon, J. Jeong, G. Li, J. Cho, and B. Lee, "One shot 360-degree light field capture and reconstruction with depth extraction based on optical flow for light field camera," Applied Sciences, vol. **8**, no. 6, article 890, 2018.
29. H. Todoroki and H. Saito, "Light field rendering with omni-directional camera," Proc. SPIE 2003, 5150, 1159–1169.
30. Y. Sando, K. Satoh, T. Kitagawa, M. Kawamura, D. Barada and T. Yatagai, "Super-wide viewing-zone holographic 3D display using a convex parabolic mirror," Sci. Rep, **8**, 2018.
31. B. Braker and E. D. Moore, "Catadioptric projector systems, devices, and methods," US Patent Application, Publication Number: US/2017/0023780/Al (Jan 2017).
32. J.-S. Jang and B. Javidi, "Three-dimensional integral imaging with electronically synthesized lenslet arrays," Opt. Lett. **27**, 1767-1769 (2002).
33. M. Hain,W. Spiegel,M. Schmiedchen, T. Tschudi, and B. Javidi, "3D integral imaging using diffractive Fresnel lens arrays," Opt. Express **13**,

315-326 (2005).

34. D. Mendlovic and A. W. Lohmann, “Space-bandwidth product adaptation and its application to superresolution: fundamentals,” J. Opt. Soc. Am. A **14**, 558–562 (1997).
35. B. L. Reddy, M. P. Phinehas and A. Nelleri, “Space bandwidth product analysis of digital holography and image reconstruction process,” 2017 International Conference on Nextgen Electronic Technologies: Silicon to Software (ICNETS2), Chennai, 2017, pp. 194-197.
36. F. Yaras, H. Kang and L. Onural, “Multi-SLM holographic display system with planar configuration,” 2010 3DTV-Conference: The True Vision - Capture, Transmission and Display of 3D Video, Tampere, 2010, pp. 1-4.
37. J.-H. Lee, J. Park, D. Nam, S. Young Choi, D.-S. Park, and C. Y. Kim, “Optimal projector configuration design for 300-Mpixel multi-projection 3D display,” Opt. Express **21**, pp. 26820-26835, 2013.
38. Apotelyth, ttps://www.apotelyt.com/compare-camera/sony-a7r-ii-vs-sony-a850, (2018).